

# D-band center modulation of B-mediated FeS<sub>2</sub> to activate molecular nitrogen for electrocatalytic ammonia synthesis

Hang Xiao, Mengyang Xia, Ben Chong, He Li, Bo Lin\*, Guidong Yang\*

XJTU-Oxford International Joint Laboratory for Catalysis, School of Chemical Engineering and Technology, Xi'an Jiaotong University, Xi'an, Shaanxi 710049, China



## ARTICLE INFO

### Keywords:

D-band center modulation  
Spin orbital  
B-mediation  
Nitrogen activation  
Electrocatalytic nitrogen fixation

## ABSTRACT

Electrocatalytic nitrogen fixation is a promising approach for ambient ammonia synthesis. The key that limits the improvement of ammonia evolution performance is the N≡N bond cleavage of molecular nitrogen. One effective route to break this bottleneck is the d-band center modulation of catalysts. Herein, a nonmetal boron mediated FeS<sub>2</sub> (B-FeS<sub>2</sub>) is developed for electrocatalytic nitrogen fixation. The B-mediation alters the spin-orbits of Fe site and upshifts the d-band center of FeS<sub>2</sub>, thus inducing a strong d-π\* interaction between the Fe site and nitrogen to activate N≡N bond. Besides, the experimental and theoretical calculations indicate the B-mediation reduces the energy barrier for \*NNH intermediate, thus significantly accelerating ammonia production. As a result, B-FeS<sub>2</sub> displays high ammonia yield (1.56 mmol·g<sup>-1</sup>·h<sup>-1</sup>) with 12.6 % Faradaic efficiency. This strategy of d-band center tuning induced by the B-mediation provides a distinctive insight for the design of high-efficiency electrocatalysts.

## 1. Introduction

Nitrogen reduction for ammonia synthesis driven by the renewable electricity has been considered as an effective method to replace the traditional Haber-Bosch process, due to the benefits of mild reaction conditions and zero carbon emissions [1–3]. However, the molecular nitrogen is difficult to be activated due to the high stability of N≡N triple bond (941 kJ mol<sup>-1</sup>), thus resulting in the low electrocatalytic nitrogen reduction reaction (eNRR) efficiency [4,5]. One promising route to break this bottleneck is the regulation of the d-band centers of catalysts and the electronic state of the reaction active sites [6,7]. The raised d-band center towards the Fermi energy level of metal-based catalysts enables the formation of the coupling between the d-orbital of metal active site and the p-orbital of nitrogen (Fig. 1), therefore allowing more d-electrons of metal active sites to fill the antibonding state of molecular nitrogen and thus forming a strong d-π\* interaction [8–11]. This interaction leads to the significant charge transfer between the molecular nitrogen and the metal active sites of catalysts, therefore accelerating the adsorption process of molecular nitrogen on the surface of catalysts [12]. More importantly, the metal-based catalysts with the higher d-band center and lower work function have the weakened electron binding confinement [13]. This means that the electrons are easier to escape from the surface of the catalysts to fill the antibonding orbitals of nitrogen to activate nitrogen. Therefore, the d-band center

modulation of metal-based catalysts is beneficial to reduce the energy barrier of N≡N triple bond cleavage, facilitate the activation of molecular nitrogen and thus enhance the eNRR performance [14]. For example, Chen et al. [15] reported a strategy to modulate the electronic structure of layered double hydroxide (LDH) by replacing copper with ferrous iron. The introduction of ferrous iron regulates the d-band center position of copper sites in this LDH material, thereby significantly improving the nitrogen adsorption to enhance eNRR activity. Tong et al. [16] constructed Pt<sub>3</sub>Fe nanocrystals via the introduction of Fe atoms into the Pt cluster. The Fe-3d band can act as the unique d-d coupling correlation center to upshift the d-band center position of Pt sites and thus facilitate the electron transfer in the Pt 5d orbitals, which significantly improves the eNRR performance of Pt<sub>3</sub>Fe (1.02 mmol·g<sup>-1</sup>·h<sup>-1</sup>). Ma et al. [17] regulated the binding ability of the reactive sites and nitrogen via introducing metal Zn into Pd, which raised the position of d-band center of the Pd sites. This strategy of optimizing d-band center of Pd sites contributes to an eNRR rate of 0.31 mmol·g<sup>-1</sup>·h<sup>-1</sup> (a Faradaic efficiency of 16.9 %).

Up to now, researches have focused on the d-band center modulation of metal-based catalysts via the introduction of metal heteroatom rather than the non-metal heteroatom [18]. It is worth noting that the non-metal heteroatoms represented by the boron atom have the unique advantages on the d-band center modulation of metal-based catalysts [19]. On one hand, the introduction of the boron heteroatom can trigger

\* Corresponding authors

E-mail addresses: [bolinsct@xjtu.edu.cn](mailto:bolinsct@xjtu.edu.cn) (B. Lin), [guidongyang@xjtu.edu.cn](mailto:guidongyang@xjtu.edu.cn) (G. Yang).

a strong hybridization between the d orbitals of the metal sites in the catalysts and the p orbitals of the boron atoms, which leads to the emergence of more gap states and the upward shift in the Fermi level of the metal sites of catalysts [20,21]. This change induces a strain in the metal-based catalysts to cause an inhomogeneous distribution of charges, thereby boosting the charge transfer and conductivity of materials [22]. On the other hand, compared to metal mediators, the introduction of non-metal can prevent the formation of the metal-H bonds and the occurrence of hydrogen evolution reaction (HER) to enhance the nitrogen fixation performance [23,24]. Hence, the d-band center modulation by virtue of the boron heteroatom is a promising method to achieve high eNRR activity for metal-based catalysts.

Pyrite ( $\text{FeS}_2$ ) has abundant active sites of nitrogen fixation and can inhibit the competitive reaction of water splitting. However, it does not display satisfactory eNRR performance due to the energy mismatching between the 3d orbitals of Fe sites and the  $2\pi^*$  orbitals of  $\text{N}_2$  [25,26]. Owing to the characteristics of  $\text{FeS}_2$  mentioned above, it can be an appropriate model material for investigating the relation between the d-band center modulation via the boron introduction and the activation of  $\text{N}\equiv\text{N}$  bond in nitrogen reduction reaction. In this work, a B-mediated  $\text{FeS}_2$  nanosheet is designed and constructed for eNRR. Combined with experiments and density functional theory (DFT), the B-mediation can cause a upshift of the d-band center of  $\text{FeS}_2$  to facilitate the activation of  $\text{N}\equiv\text{N}$  bond of  $\text{N}_2$  and accelerate the first step of hydrogenation in the rate-determining step of eNRR. As a result, the B- $\text{FeS}_2$  shows high ammonia yield ( $1.56 \text{ mmol}\cdot\text{g}^{-1}\cdot\text{h}^{-1}$ ) with 12.6 % FE at  $-1.4 \text{ V}$  vs.  $\text{Ag}/\text{AgCl}$ . This indicates that B-mediated  $\text{FeS}_2$  is a promising eNRR catalyst, which is evidenced by the comparison of the advantages and drawbacks with other state-of-the-art eNRR catalysts in Supporting Information.

## 2. Experimental section

### 2.1. Synthesis of $\text{FeOOH}$ nanosheets

$\text{FeOOH}$  nanosheets were prepared via the water-bath method. Specifically, 0.1 M of  $\text{FeSO}_4\cdot7\text{H}_2\text{O}$  and 0.1 M of  $\text{CH}_3\text{COONa}$  were dissolved in 40 mL of  $\text{H}_2\text{O}$  and continuously stirred at  $40^\circ\text{C}$  for 2 h to obtain the precursor of  $\text{FeOOH}$  nanosheets. Then the precursor was washed and dried under  $60^\circ\text{C}$  for 12 h.

### 2.2. Synthesis of $\text{Fe}_2\text{O}_3$ nanosheets

$\text{Fe}_2\text{O}_3$  nanosheets were obtained via the high-temperature

calcination of the precursor of  $\text{FeOOH}$  nanosheets. In the typical experiment, the obtained  $\text{FeOOH}$  nanosheets were placed in a porcelain boat and calcined in a muffle furnace at  $300^\circ\text{C}$  for 2 h with a heating rate of  $5^\circ\text{C}\cdot\text{min}^{-1}$  under the air atmosphere.

### 2.3. Synthesis of $\text{FeS}_2$ and B mediated $\text{FeS}_2$ nanosheets

The B mediated  $\text{FeS}_2$  was prepared by the sulfidation treatment at high temperature in a tube furnace. Typically, 50 mg of  $\text{Fe}_2\text{O}_3$ , 100 mg of sulfur powder and a certain amount of  $\text{H}_3\text{BO}_3$  were successively added to the mortar and ground for 5 min. The mixed powder was placed in a porcelain boat and calcined in a tube furnace at  $500^\circ\text{C}$  for 2 h under the nitrogen atmosphere. A series of B- $\text{FeS}_2$  samples with the different mass ratios of 200:50, 250:50, 300:50 and 350:50 samples were prepared and labelled ad B- $\text{FeS}_2$ -4, B- $\text{FeS}_2$ -5, B- $\text{FeS}_2$  as well as B- $\text{FeS}_2$ -7, respectively. For comparison, the pure  $\text{FeS}_2$  was synthesized by the similar synthetic process without the addition of  $\text{H}_3\text{BO}_3$ , which is labelled as  $\text{FeS}_2$ .

### 2.4. Characterization

The prepared samples were investigated through various instruments. The scanning electron microscope and transmission electron microscope (Talos F200X) equipped with an energy dispersive spectrometer (EDS) were applied to analyze the structure and morphology of obtained samples. Besides, the scanning transmission electron microscope (STEM) was obtained via a FEI Themis Z electron microscope. X-ray diffraction (XRD-6100, SHIMADZU) was used to explore the crystal phases of the as-synthesized samples. The chemical state of the as-prepared samples surface was determined by the time-dependent X-ray photoelectron spectroscopy (XPS) with an ESCALAB 250 spectrometer (Thermo Electron Corporation). The Chemisorption apparatus (Autosorb-iQC-TPX) was used to measure the temperature programmed desorption (TPD) of the synthetic samples. The Brunauer-Emmett-Teller (BET) specific surface areas and pore size were detected by using the Barrett-Joyner-Halenda (BJH) methods.

### 2.5. Electrode preparation

In a typical experiment, 6 mg of the as-prepared catalyst was added to 1 mL of ethanol contained 5 vol% Nafion solution. And the mixture was sonicated for 20 min to obtain a homogeneous slurry. Subsequently, 50  $\mu\text{L}$  of the prepared slurry was loaded on a carbon paper ( $1 \text{ cm}^2$ ) electrode and dried.

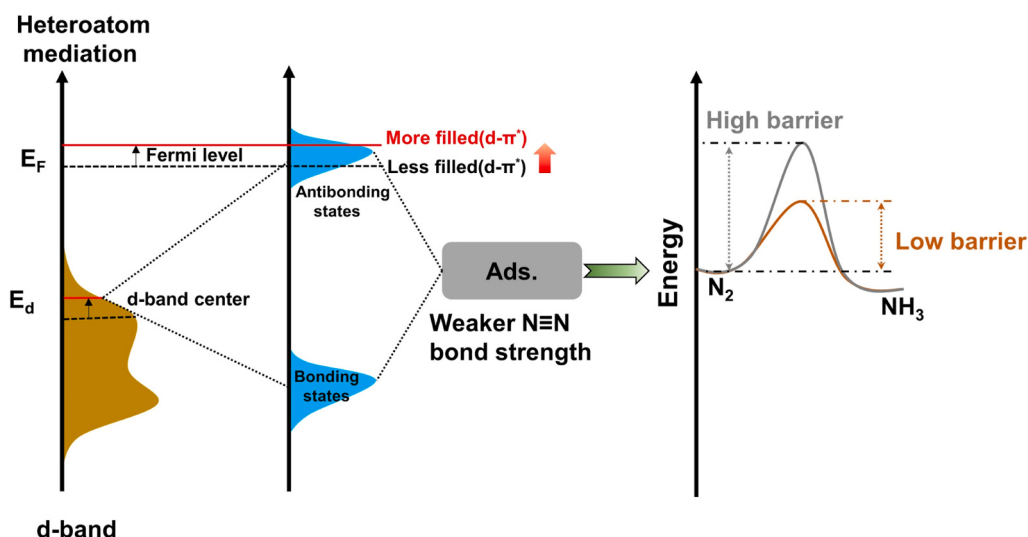


Fig. 1. The mechanism diagram of the upshifting of the d-band center related to metal-based catalysts for boosting nitrogen reduction.

## 2.6. Electrochemical measurement

All tests were investigated by the electrochemical analyzer (AMETEK, PMC-1000/DC) with a standard three-electrode system. For the electrochemical active surface area (ECSA) test, the prepared electrode served as the working electrode, while an Ag/AgCl electrode (3 M KCl) was used as the reference electrode. A carbon rod was employed as the counter electrode, and the methanol solution of 0.1 M KOH was used as the electrolyte. For the electrochemical impedance test, 1 mg of catalyst was added to 200  $\mu$ L of ethanol contained 10 vol% Nafion and sonicated for 30 mins. Then the solution mentioned above was loaded on ITO glass as the working electrode, Ag/AgCl (3 M KCl) electrode was used as the reference electrode. Carbon rod was used as the counter electrode, and the 1 M Na<sub>2</sub>SO<sub>4</sub> solution was used as the electrolyte.

## 2.7. Electrocatalytic nitrogen reduction reaction

The electrocatalytic nitrogen reduction reaction was conducted in a H-type cell applied as the electrolytic tank. Firstly, the cathode and anode of the H-type cell were added with 30 mL of 0.1 M KOH methanol solution containing 0.16 vol% H<sub>2</sub>O, and the absorption solution consisted of 30 mL of 0.1 M HCl. Subsequently, the pure N<sub>2</sub> gas was purged into 100 mL of 1 M H<sub>2</sub>SO<sub>4</sub> and 100 mL of 1 M KOH to remove potential NO<sub>x</sub> and NH<sub>3</sub>. Finally, the nitrogen was fluxed into the H-type cell for 30 min to reach saturation in the electrolyte before electrocatalytic testing. As a contrast, the blank experiment follows the similar process in Ar atmosphere.

The Faradaic efficiency (FE) of the as-prepared samples were investigated under the same experimental conditions as above. The FE for ammonia was calculated using the following equation  $FE = (3 F \times n \times V) / (17 \times Q)$ , where F represents the Faraday's constant, n is the concentration of ammonia generated, Q represents the amount of charge, and V represents the volume of electrolyte. Three independent tests were carried out to calculate the error bars of the eNRR activity.

## 2.8. Determination of ammonia production

The ammonia produced was quantitatively detected by the common spectrophotometric indophenol blue method. Briefly, the electrolytic solution after the cathodic electrolytic cell reaction and the adsorbing solution were mixed and rotary evaporated to obtain NH<sub>4</sub>Cl product. After that, 10 mL of ultrapure water was added to obtain a product solution. Then, a indophenol blue method was used to measure the ammonia content. Concretely, the NaOH solution containing 5 wt% sodium citrate and 5 wt% salicylic acid (2 mL), 0.5 M NaClO solution (1 mL) and 1 wt% Na<sub>2</sub>[Fe(CN)<sub>5</sub>NO] solution (0.2 mL) were sequentially added to 2 mL of the sample to be tested, which was shaken, left to stand in a dark place for 2 h, and then its absorbance at a wavelength of ~657 nm was measured via UV-vis diffuse reflection spectra. The ammonia content was calculated by the absorbance of a series of standard liquids with different concentrations of ammonia. The ammonia yield was calculated as following:  $r = (c \times v) / (t \times m)$ , where c is the concentration of ammonia produced ( $\text{mol} \cdot \text{L}^{-1}$ ), v represents the volume of the product solution (L), t is the reaction time (h), and m is the catalyst content (g).

## 2.9. Determination of hydrazine hydrate

The possible by-product of N<sub>2</sub>H<sub>4</sub> can be measured by the Watt and Chrissp method. In a typical experiment, 300 mL of ethanol, 30 mL of concentrated hydrochloric acid and 5.99 g of p-C<sub>9</sub>H<sub>11</sub>NO were used to obtain the color reagent. The 5 mL of the product solution was mixed with the 5 mL of as-prepared color reagent and stayed at room temperature for 20 mins. If the N<sub>2</sub>H<sub>4</sub> was generated in the reaction solution, it can react with the p-C<sub>9</sub>H<sub>11</sub>NO to form a yellow azo compound under

the acidic conditions. More importantly, the absorbance of the mentioned azo compound containing N<sub>2</sub>H<sub>4</sub> can be recorded at a wavelength of ~455 nm in the UV-visible diffuse reflectance spectra (DRS). The content of the generated N<sub>2</sub>H<sub>4</sub> was quantitatively calculated according to the standard curve of N<sub>2</sub>H<sub>4</sub> at in the UV-visible DRS.

## 2.10. In-situ FTIR

A Pt wire was used as the counter electrode, Ag/AgCl as the reference electrode, and the ink of catalyst was coated on the glassy carbon electrode as the working electrode. Electrochemical in-situ FTIR was carried out by a Bruker INVENIO FTIR spectrometer equipped with an MCT detector and a CaF<sub>2</sub> light window via the external reflection mode. Before the test, the high purity nitrogen was aerated for half an hour in nitrogen-methanol co-electrolysis system to reach nitrogen saturation. All the spectra were scanned for 16 times. All backgrounds were acquired without the applied external potential.

## 2.11. DFT calculation

The first-principles calculations were realized through the Vienna Ab Initio Simulation Package (VASP). To describe the effects of exchange correlation and on-site Coulomb interactions, we utilize a generalized gradient approximation (GGA) and the Perdew-Burke-Ernzerhof (PBE) in VASP with Hubbard + U correction. Where the Ueff value is 2 eV and is described as van de Waals using empirical corrections in the Grimme scheme (DFT + D2). The plane wave cut-off energy is 520 eV. The Cubic FeS<sub>2</sub> with the space group of Pa-3 (205) was used. The calculation model consists of 72 atoms. The convergence criteria for the total energy and the Hellmann-Feynman force are  $10^{-7}$  eV and  $0.02 \text{ eV} \cdot \text{\AA}^{-1}$ , respectively. In order to accurately describe the electrons and magnetism of FeS<sub>2</sub>, its antiferromagnetic structure has been considered, using MAGMOM of 4. And combined with XRD and HRTEM analysis, the exposed (200) plane of FeS<sub>2</sub> lattice was used as the reaction surface. A Monkhorst-Pack  $5 \times 5 \times 1$  k-point grid was utilized to sample the Brillouin zone with a vacuum thickness of 25 Å. The proton-coupled electron transfer (PCET) technique is used. The computational hydrogen electrode (CHE) model is used as the reference for all Gibbs free energy values. The H<sup>+</sup>/e<sup>-</sup> pair is considered to have a half as much chemical potential as the H<sub>2</sub> gas molecule. The formula for calculating gas pressure is  $G = E + ZPE - TS$ , where E is the reaction energy difference between products and reactants that occurs on the catalyst. When the vibrational frequency is considered, ZPE and S represent the zero-point energy and entropy changes at 298.15 K, respectively.

## 3. Results and discussion

### 3.1. Morphology and crystal phase structure of catalysts

The synthesis process of B-mediated FeS<sub>2</sub> is obtained via a two-step calcination method (Fig. 2a). During the sulfidation process, the part of S atoms were replaced by B atoms to form Fe-B bond in FeS<sub>2</sub>, thereby obtaining B-mediated FeS<sub>2</sub>. The morphology of B-FeS<sub>2</sub> was analyzed by SEM, STEM and TEM. As shown in Fig. 2b and Fig. S1c, both B-FeS<sub>2</sub> and FeS<sub>2</sub> exhibit the typical nanosheet microstructure, which are similar in the structure of the precursors of FeOOH and Fe<sub>2</sub>O<sub>3</sub> (Fig. S1a,b and Fig. S2). Fig. 2c shows the high-resolution TEM (HRTEM) image of B-FeS<sub>2</sub>. It could be clearly observed that the lattice distance of B-FeS<sub>2</sub> is 0.271 nm, belonging to the (200) crystal plan of the cubic FeS<sub>2</sub>. The corresponding energy dispersive spectra (Fig. 2d) of B-FeS<sub>2</sub> confirmed that S, Fe and B elements are uniformly distributed in space, suggesting of the successful construction of boron in the FeS<sub>2</sub> nanosheets. The content of B in FeS<sub>2</sub> is 0.8 wt% through inductively coupled plasma mass spectrometry (ICP-MS) (Table S1).

The phase and crystal structure of as-prepared samples were investigated by X-ray diffraction (XRD). As shown in Fig. 2e and Fig. S3a, all

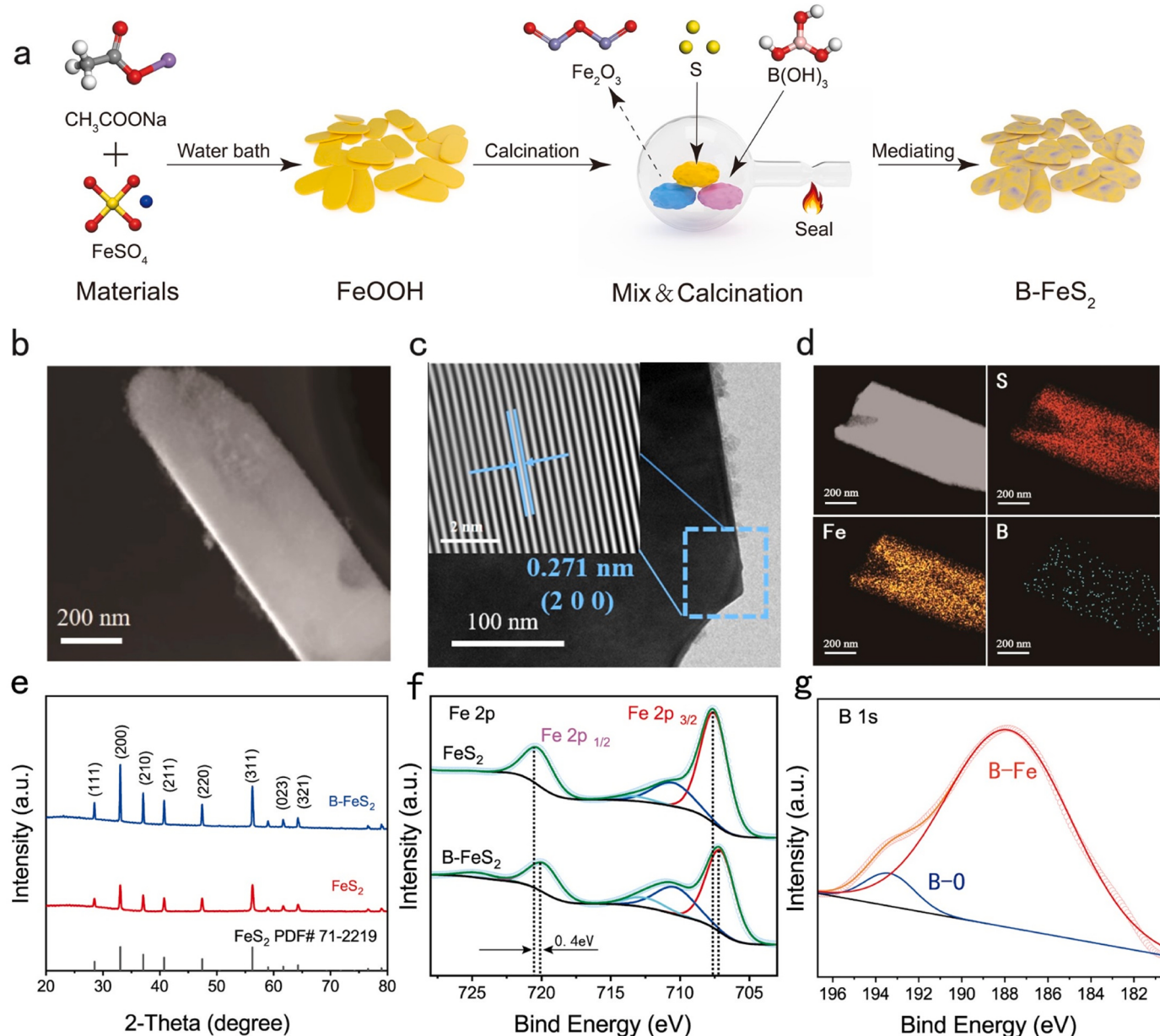


**Fig. 2.** (a) Schematic diagram of the preparation process for B-mediated FeS<sub>2</sub> nanosheets. (b) TEM, (c) HRTEM and (d) TEM images of the B-FeS<sub>2</sub> and the corresponding mapping images of the elements of S, Fe and B, (e) XRD patterns of the FeS<sub>2</sub> and B-FeS<sub>2</sub>. The XPS spectrum of samples (f) Fe 2p and (g) B 1 s.

XRD peaks belong to the cubic FeS<sub>2</sub> (JCPDS, No. 71-2219). Notably, the XRD peaks of B-FeS<sub>2</sub> are more sharp than of FeS<sub>2</sub>, indicating the improved crystallinity due to the introduction of B element. Besides, by contrast with FeS<sub>2</sub>, the XRD peaks of B-FeS<sub>2</sub> are shifted to the high-angle direction with the increased content of B (Fig. S3b). This is because the B atoms with the relatively small atomic radius replace some of S atoms in FeS<sub>2</sub>. Additionally, to further investigate the electronic structure of the B-FeS<sub>2</sub> catalyst, the chemical state of the surface of B-FeS<sub>2</sub> and pure FeS<sub>2</sub> were characterized by X-ray photoelectron spectroscopy (XPS). As displayed in Fig. S4, the two characteristic peaks at 162.6 eV and 163.9 eV in the S 2p region of pure FeS<sub>2</sub> correspond to S 2p<sub>3/2</sub> and S 2p<sub>1/2</sub>, respectively. However, the two peaks at 162.3 eV and 163.6 eV of B-FeS<sub>2</sub> are ascribed to S 2p<sub>3/2</sub> and S 2p<sub>1/2</sub>, respectively, which shifted 0.3 eV to the low binding energy compared with that of pure FeS<sub>2</sub> owing to the B introduction [27]. For Fe 2p region (Fig. 2f), the XPS peaks of B-FeS<sub>2</sub> at 707.3 eV and 720.1 eV belong to Fe 2p<sub>3/2</sub> and Fe 2p<sub>1/2</sub>, respectively. The lowered binding energy compared with pure FeS<sub>2</sub>

(707.7 eV, 720.5 eV) is due to the mediation of low-electronegativity B, which enables the adjacent Fe atoms to show the electron-rich state [28]. As shown in Fig. 2g, the faint peaks were detected in B-mediated FeS<sub>2</sub>, which is related to B 1 s. Besides, the peaks at 187.8 eV and 193.1 eV correspond with Fe-B bond in B-FeS<sub>2</sub>, further confirming the successful mediation of B into FeS<sub>2</sub> nanosheets [29,30].

### 3.2. Electrocatalytic nitrogen reduction performances of catalysts

The eNRR performances of samples were investigated in an H-type electrolytic cell with the nitrogen-saturated electrolyte. The nitrogen-methanol co-electrolysis system was used to significantly reduce the overpotential of the anodic reaction (Fig. S5). The generated NH<sub>4</sub><sup>+</sup> was measured spectrophotometrically with the indophenol blue and quantified by the calibration NH<sub>4</sub><sup>+</sup> curve (Fig. S6). The eNRR performances of B-mediated FeS<sub>2</sub> catalysts with different B amounts were investigated in Fig. S7 to find out the best sample with the optimal B content. As shown

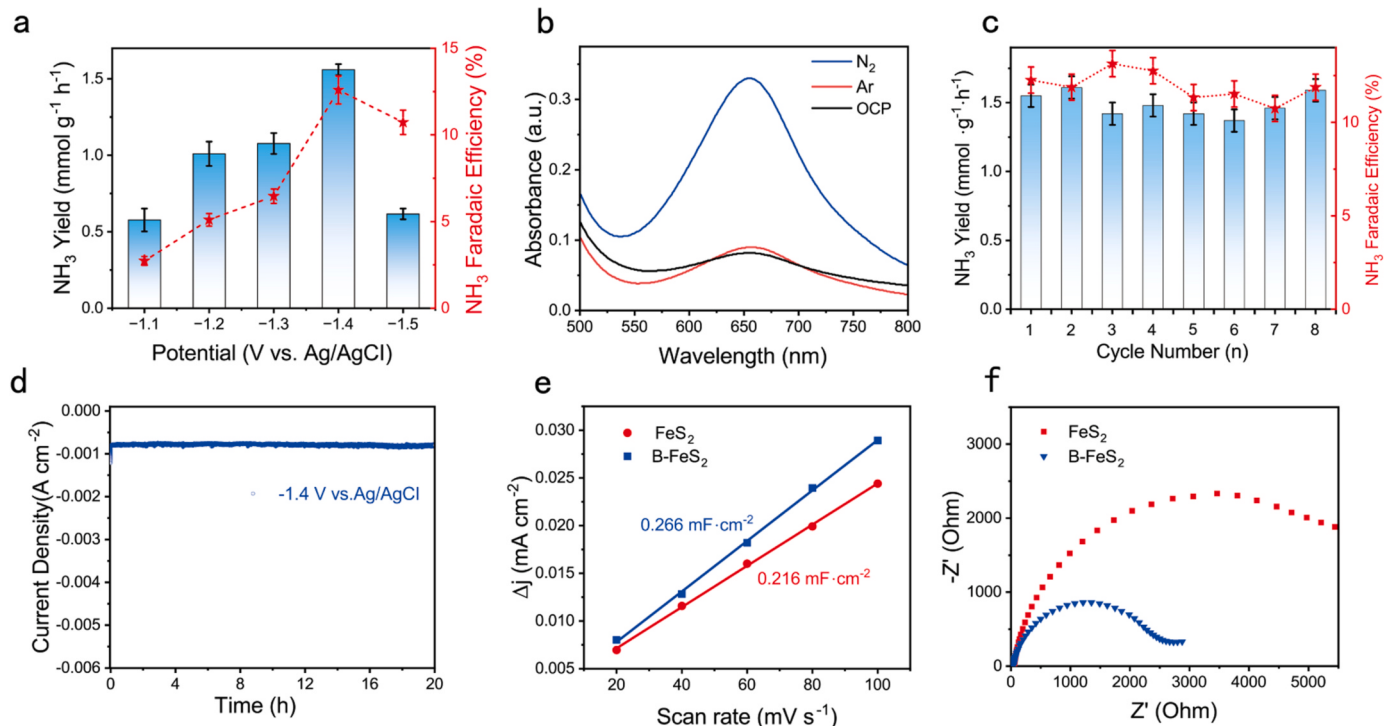


**Fig. 3.** (a) Ammonia yield and Faradaic efficiency of B-FeS<sub>2</sub> at different potentials. (b) Absorbance of B-FeS<sub>2</sub> in UV-Vis spectra under nitrogen, argon and open circuit potential (OCP) conditions. (c) Cyclic stability, (d) Time-dependent current density of B-FeS<sub>2</sub> at -1.4 V vs. Ag/AgCl. (e) The ECSA, (f) EIS Nyquist plot of B-FeS<sub>2</sub> and pure FeS<sub>2</sub> catalysts.

In Fig. 3a and Fig. S8, the eNRR rate of the optimal B-FeS<sub>2</sub> sample reached 1.56 mmol·g<sup>-1</sup>·h<sup>-1</sup> with a Faradaic efficiency of 12.6 % at -1.4 V vs. Ag/AgCl, outperforming many reported catalysts (Table S2). The outstanding eNRR performance of B-FeS<sub>2</sub> is evidenced by linear sweep voltammetry curves (Fig. S9). Besides, this conclusion is also proved by the activity tests of B-FeS<sub>2</sub> in the Ar atmosphere and open-circuit potential (Fig. 3b). As expected, NH<sub>3</sub> was formed only under nitrogen, suggesting that the source of generated ammonia in the electrolyte is derived from nitrogen. Stability is an important factor in evaluating catalyst performance. In Fig. 3c and Fig. S10, the prepared B-FeS<sub>2</sub> catalyst showed no significant decrease in ammonia yield and Faradaic efficiency after the eight cycle tests. In addition, as shown in Fig. 3d, the current density has no obvious decay after the 20 h eNRR reaction, indicating the good stability of the B-FeS<sub>2</sub> catalyst, as evidenced by the XRD pattern of B-FeS<sub>2</sub> after the reaction (Fig. S11).

The eNRR performance is directly related to the reactive sites of the catalysts. The reactive sites determine the amount of nitrogen adsorption activation, and the Electrochemical Active Surface area (ECSA) can directly reflect the number of catalytic active sites. The ECSA of B-FeS<sub>2</sub> and pure FeS<sub>2</sub> were obtained via the Cyclic Voltammetry (CV) at different scanning speeds (Fig. S12). And as shown in Fig. 3e, compared with pure FeS<sub>2</sub> (0.216 mF·cm<sup>-2</sup>), the ECSA value of B-FeS<sub>2</sub> can reach up to 0.266 mF·cm<sup>-2</sup>, indicating that the B mediation can induce more active sites to participate in the reaction, thereby enhancing the eNRR performance. In addition, the adsorption and desorption isothermal curves of nitrogen were tested. As displayed in Fig. S13 and Table S3, B-FeS<sub>2</sub> shows the larger specific surface area and increased pore volume compared with pure FeS<sub>2</sub>. It is because the precursor decomposition of H<sub>3</sub>BO<sub>3</sub> at high temperatures can produce gas to cause the increased specific surface area of B-FeS<sub>2</sub>. Additionally, the charge transfer resistance of catalysts is revealed by the electrochemical impedance spectroscopy (EIS). As shown in Fig. 3f and Fig. S14, the charge transfer resistance of B-FeS<sub>2</sub> was significantly decreased than that of FeS<sub>2</sub>, suggesting the boosted charge transfer capability induced by the introduction of B atoms [31–33].

Besides, the nitrogen adsorption capacity of catalysts was detected by temperature programmed desorption isotherms (TPD) under N<sub>2</sub> atmosphere. As displayed in Fig. S15a, the chemical desorption temperature of B-FeS<sub>2</sub> is 557 °C, which is higher than that of pure FeS<sub>2</sub> (540 °C), indicating that B-FeS<sub>2</sub> requires a higher temperature to surmount the desorption of N<sub>2</sub> [34]. In addition, the TPD of NH<sub>3</sub> was also examined. As in Fig. S15b, the desorption temperature of B-FeS<sub>2</sub> for ammonia is lower than that of pure FeS<sub>2</sub>, manifesting that B-FeS<sub>2</sub> can desorb the product ammonia in time to release the active sites. Moreover, the adsorption energy of nitrogen on B-FeS<sub>2</sub> and pure FeS<sub>2</sub> were calculated by DFT. As shown in Fig. S16, the adsorption energy of B-FeS<sub>2</sub> for nitrogen is -1.15 eV, which is higher than that of pure FeS<sub>2</sub> (-0.88 eV). This indicates the strong nitrogen adsorption energy of B-FeS<sub>2</sub>, corresponding to the N<sub>2</sub>-TPD conclusion.

### 3.3. The influence of d-band center modulation for B-FeS<sub>2</sub> on the generation of intermediates and eNRR performance

To explore the action of d-band center modulation on the generation of intermediates in eNRR process, the catalytic pathway of B-FeS<sub>2</sub> was investigated through in-situ FTIR spectroscopy. As shown in Fig. 4a, the intensity of the characteristic peaks related to -N-N and -N = N bonds becomes stronger with the increasing reaction time during the eNRR process, revealing the cleavage of the N≡N bond on the surface of catalyst [35,36]. The peaks at 1330 cm<sup>-1</sup>, 1520 cm<sup>-1</sup> and 1420 cm<sup>-1</sup> were attributed to the characteristic peaks of adsorbed NH<sub>3</sub> and asymmetric deformation vibrations of NH<sub>4</sub><sup>+</sup>, respectively, suggesting the generation of ammonia in the eNRR process [37]. In addition, the characteristic peaks at 1090 cm<sup>-1</sup> and 1620 cm<sup>-1</sup> were attributed to the vibrations of the intermediate -NH<sub>2</sub> and -N-H in the eNRR process, respectively [38,39]. Moreover, the in-situ FTIR spectroscopy of pure FeS<sub>2</sub> was also tested under the same conditions. As shown in Fig. S17, the intensity related to the peaks of intermediates and produced ammonia in B-FeS<sub>2</sub> is significantly higher than that of pure FeS<sub>2</sub>, suggesting that B-FeS<sub>2</sub> can produce more intermediates under the eNRR

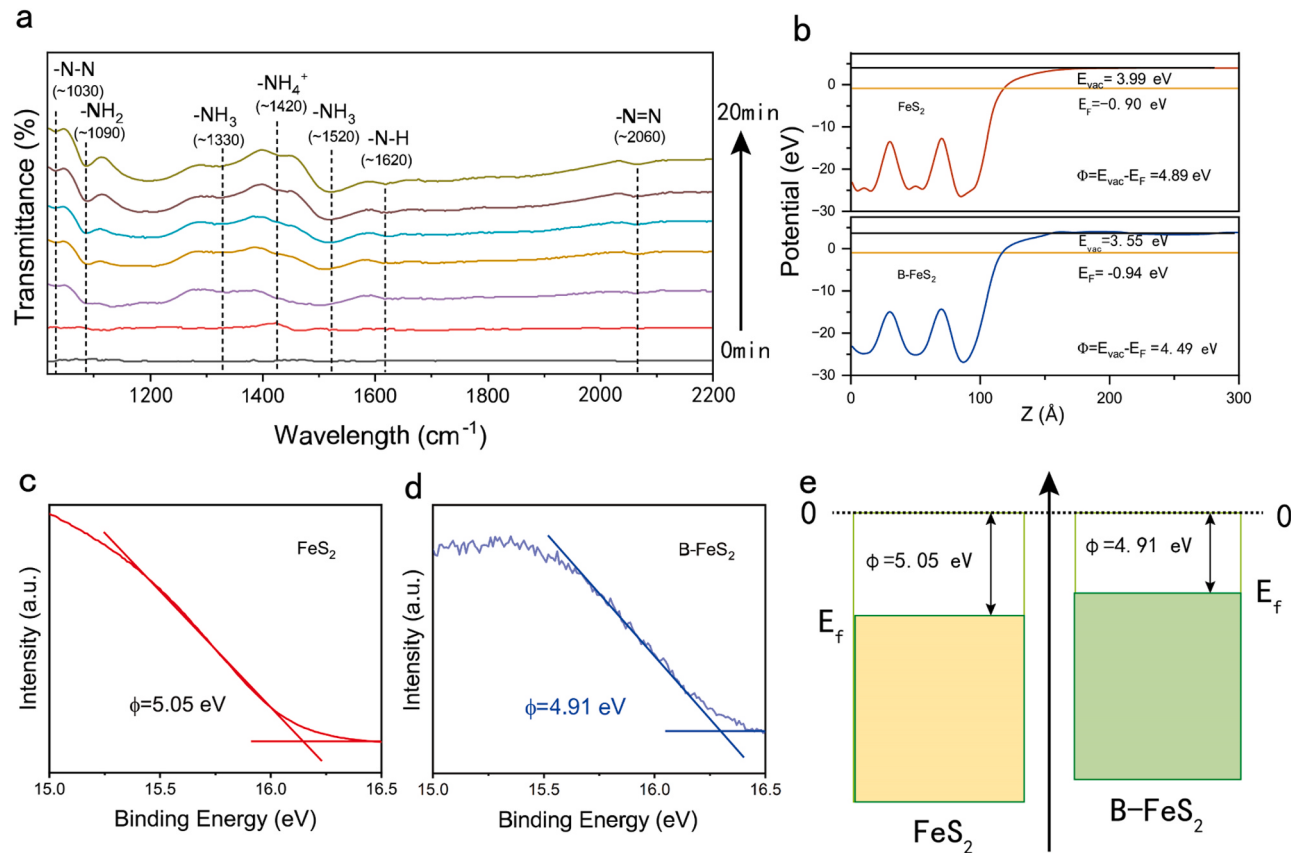


**Fig. 4.** (a) In-situ FTIR spectra of B-FeS<sub>2</sub>. (b) The corresponding work functions of FeS<sub>2</sub> and B-FeS<sub>2</sub> calculated by DFT. UPS spectra corresponding to the work function of (c) Pure FeS<sub>2</sub> and (d) B-FeS<sub>2</sub>. (e) The schematic of the work functions of pure FeS<sub>2</sub> and B-FeS<sub>2</sub>.

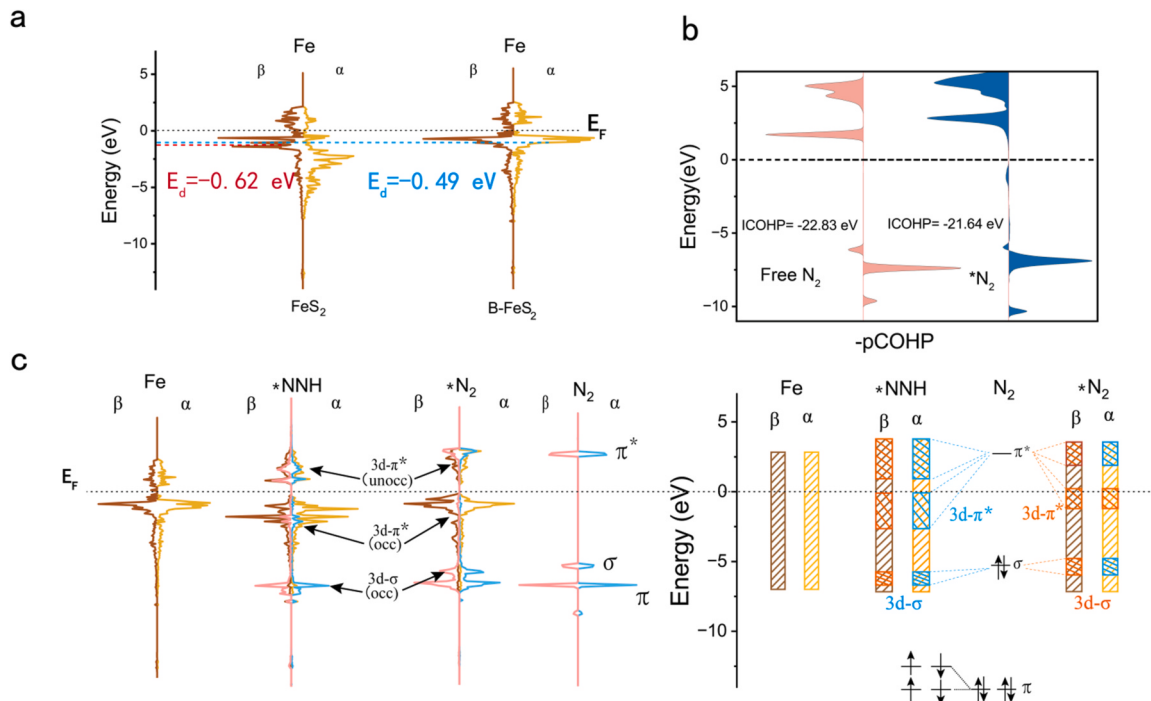


**Fig. 5.** (a) Projected electronic densities of states (PDOS) related to 3d orbitals and d-band center of the Fe sites over pure FeS<sub>2</sub> and B-FeS<sub>2</sub>. (b) The computed pCOHP of free N<sub>2</sub> and  ${}^*\text{N}_2$  on B-FeS<sub>2</sub>. (c) PDOS related to the interaction between the d orbitals of the Fe sites and the nitrogen molecules.

process. This phenomenon strongly evidences that the eNRR kinetics of B-FeS<sub>2</sub> is faster than that of FeS<sub>2</sub> due to the raised d-band center of Fe sites [40], which is beneficial to improve the eNRR activity.

To further illustrate the relationship between the B mediation and the change in the d-band center of FeS<sub>2</sub>, the work function of FeS<sub>2</sub> and B-FeS<sub>2</sub> were calculated by DFT calculations. As displayed in Fig. 4b, the work function of B-FeS<sub>2</sub> (4.49 eV) was lower than that of FeS<sub>2</sub> (4.89 eV) calculated by DFT. This conclusion is proved by the ultraviolet photo-electron spectroscopy (UPS). As displayed in Fig. 4c,d and Fig. S18, the work function of B-FeS<sub>2</sub> is 4.91 eV, while the work function of pure FeS<sub>2</sub> is 5.05 eV. These indicate that B mediation can effectively reduce the work function of FeS<sub>2</sub>, thus leading to a higher Fermi energy level and d-band center energy level of B-FeS<sub>2</sub>. Combined with the experimental and calculation results presented above, the lowered work function of B-FeS<sub>2</sub> suggests the higher  $E_d$  energy level compared with FeS<sub>2</sub>. This indicates that the binding energy of high-energy electrons regarding the Fe sites in B-FeS<sub>2</sub> become weak, so more high-energy electrons can participate in the eNRR reaction (Fig. 4e).

To explore the reason that B mediation can upshift the d-band center of FeS<sub>2</sub>, we carried out the theoretical calculations on the projected electronic densities of states (PDOS) related to the 3d orbitals of Fe sites in pure FeS<sub>2</sub> and B-FeS<sub>2</sub>. Fig. 5a shows that the B atoms mainly modulate the spin-up electronic state of the Fe sites, and the spin-up electrons shifted up nearly to the Fermi energy level of FeS<sub>2</sub>, thus mediating the d-band center of B-FeS<sub>2</sub>. Furthermore, the PDOS also shows that the d-band center of pure FeS<sub>2</sub> is -0.62 eV, while the d-band center of B-FeS<sub>2</sub> is -0.49 eV, manifesting an upshift of 0.13 eV from FeS<sub>2</sub> to B-FeS<sub>2</sub>. To investigate the effect of the raised d-band center on the nitrogen activation, the projected crystal orbital Hamilton population (pCOHP) of B-FeS<sub>2</sub> was studied. As exhibited in Fig. 5b, the bonding contribution is on the right while the antibonding contribution is on the left. It is clearly shown that the antibonding orbitals of free nitrogen near the Fermi level are not filled with electrons, but the antibonding orbitals of nitrogen adsorbed on surface of B-FeS<sub>2</sub> near the Fermi level display obvious electron filling states, suggesting that nitrogen is activated. Additionally, compared with free nitrogen (22.83 eV), the absolute ICOHP value related to the nitrogen adsorbed on surface of B-FeS<sub>2</sub> (21.64 eV) is lower, suggesting that the electrons of B-FeS<sub>2</sub> can effectively transfer to the antibonding orbitals of nitrogen to activate N<sub>2</sub> [41].

Furthermore, according to the d-band center theory, when the chemisorption occurs on the metal sites, the d orbitals of the metal sites can interact with the adsorbed reactant molecules to form the bonding and antibonding states. The position of the d-band center determines the extent to which the antibonding states are filled with electrons, which in turn determines the stability of the bonding and the strength of the adsorption. As shown in Fig. 5c, the 3d orbital of Fe can match with the  $\pi^*$  orbital of nitrogen, thus forming the partially occupied 3d- $\pi^*$  (occ) orbitals. With the construction of the 3d- $\pi^*$  orbitals, the electrons from Fe 3d orbital can transfer to the empty  $\pi^*$  orbital of the nitrogen, therefore activating the N≡N bond of N<sub>2</sub>. Moreover, other formed unoccupied 3d- $\pi^*$  (unocc) antibonding orbitals located above the Fermi energy level leading to the increased adsorption strength of N<sub>2</sub> for the Fe sites in B-FeS<sub>2</sub>. After the N<sub>2</sub> is effectively activated, the \*N<sub>2</sub> can react with H<sup>+</sup> in reaction solution to form \*NNH, the 3d orbitals of Fe overlap with the  $\pi^*$  orbitals of \*NNH, thus further weakening the N≡N triple bond of N<sub>2</sub> [42,43]. In addition, the 3d- $\sigma$  (occ) orbital bonding state is about 0.15 eV, which is smaller than the  $\delta$  orbital of the nitrogen, indicating that the nitrogen is further activated. As a result, in the subsequent continuous hydrogenation process, Fe and H atoms can continuously provide electrons to the empty  $\pi^*$  orbitals of nitrogen, therefore facilitating the process of nitrogen hydrogenation to ammonia production.

### 3.4. The eNRR mechanism of catalysts

To further demonstrate the nitrogen activation by Fe sites. The

electron localization functions (ELF) and charge density differences related to nitrogen adsorption on the Fe sites were examined. Compared with nitrogen adsorbed onto pure FeS<sub>2</sub> (Fig. S19), the negative charges are mainly concentrated on the adsorbed nitrogen molecules, thus forming a significant charge accumulation in Fig. 6a [44,45]. In addition, there is charge transfer between the Fe sites and nitrogen molecules, which indicates that the Fe site transfers electrons to the empty  $\pi^*$  orbital of N<sub>2</sub> (Fig. 6b process 1). Besides, the lone pair of electrons from nitrogen is injected into the empty d orbital of Fe (Fig. 6b process 2), thus activating the N≡N bond and boosting the eNRR performance. Additionally, Bader Charge of the Fe sites in pure FeS<sub>2</sub> and B-FeS<sub>2</sub> was calculated (Fig. S20). After the B mediation, the Bader Charge of Fe sites changed from 0.645 |e| to 0.502 |e|, suggesting that the B atoms modulate the electronic structure of Fe to the electron-rich state, which is consistent with Fig. 2f. Besides, the Bader Charge of the dinitrogen molecule and the bond length for N≡N triple bond were calculated during the eNRR hydrogenation according to the alternating path. As shown in Fig. 6c, the Bader Charge of the dinitrogen molecule adsorbed on FeS<sub>2</sub> (\*N<sub>2</sub> + H<sup>+</sup> + e<sup>-</sup> = \*NNH) is 0.351 |e|, while the Bader Charge on B-FeS<sub>2</sub> increases significantly to 0.499 |e|, demonstrating that the dinitrogen molecule is well activated on B-FeS<sub>2</sub> [46]. In addition, the bond length of the dinitrogen molecule also changed from 1.186 Å to 1.219 Å in Fig. S21, which is favorable for the following eNRR process.

The eNRR reaction mechanism of nitrogen on FeS<sub>2</sub> and B-FeS<sub>2</sub> was investigated. The complex mechanism indicates that the eNRR reaction is a multi-step electron-coupled proton process. As shown in Fig. S22, the adsorption of nitrogen molecule on the surface of FeS<sub>2</sub> and B-FeS<sub>2</sub> is a spontaneous process. Furthermore, when comparing the distal pathway with the alternating pathway, there is a significant uphill energy barrier (\*NNH<sub>2</sub> + H<sup>+</sup> + e<sup>-</sup> = \*N + NH<sub>3</sub>) for the pure FeS<sub>2</sub> and B-FeS<sub>2</sub> systems in the distal pathway. This suggests that the pure FeS<sub>2</sub> and B-FeS<sub>2</sub> systems face huge challenges in the following distal pathway during eNRR process from the thermodynamical respect. Consequently, the eNRR reaction on both FeS<sub>2</sub> and B-FeS<sub>2</sub> is inclined to occur via the alternating pathway. Moreover, as displayed in Fig. 6d, compared with pure FeS<sub>2</sub> (-0.337 eV), nitrogen is more readily adsorbed on B-FeS<sub>2</sub> due to the lower adsorption energy (-0.501 eV), corresponding with Fig. S15 and Fig. S16. It is noteworthy that the first hydrogenation step (\*NN + H<sup>+</sup> + e<sup>-</sup> = \*NNH) exhibits the highest energy barrier in the eNRR processes over pure FeS<sub>2</sub> and B-FeS<sub>2</sub>. This indicates that the first hydrogenation step is the rate-determining step (RDS) for the eNRR route. Furthermore, to verify this conclusion, the proton source in the electrolyte was replaced by D<sub>2</sub>O, the eNRR performance and LSV curves are shown in Fig. S23. It can be observed that a significant decrease trend occurs on the eNRR performance, FE as well as the current density after the replacement of water by D<sub>2</sub>O. This is due to the difference in the mass of H/D and the vibration frequency of the bond [47]. The kinetic isotope effect (KIE) value of B-FeS<sub>2</sub> is about 3.18, which is consistent with the characteristics of primary KIE [48]. These results indicate that B-FeS<sub>2</sub> significantly accelerates the activation of N<sub>2</sub> and the first step of hydrogenation [49]. Nevertheless, B-FeS<sub>2</sub> exhibits a markedly different value of  $\Delta G$  (0.519 eV) in the first hydrogenation step compared with pure FeS<sub>2</sub> (1.201 eV), resulting in the energy barrier of B-FeS<sub>2</sub> is relatively lowered by 0.682 eV. It is because B-FeS<sub>2</sub> can transfer more d electrons to the antibonding orbitals of nitrogen and elongate the nitrogen-nitrogen triple bond (Fig. 6c and Fig. S21), thus effectively activating nitrogen molecule and lowering the energy barrier for the eNRR process. Moreover, The intermediate N<sub>2</sub>H<sub>4</sub> was experimentally detected by the spectrophotometric experiment to verify the reaction pathway [50]. The N<sub>2</sub>H<sub>4</sub> intermediate was detected in the electrolyte after 2 h reaction over B-FeS<sub>2</sub> (Fig. S24 and Fig. S25), suggestive of an alternating pathway occurred (Table S4).

According to all results presented above, the B-mediation alters the spin-orbits of Fe site and upshifts the d-band center of FeS<sub>2</sub>, therefore inducing a strong d- $\pi^*$  interaction between the Fe site and nitrogen to activate N≡N bond. Moreover, the experimental and theoretical

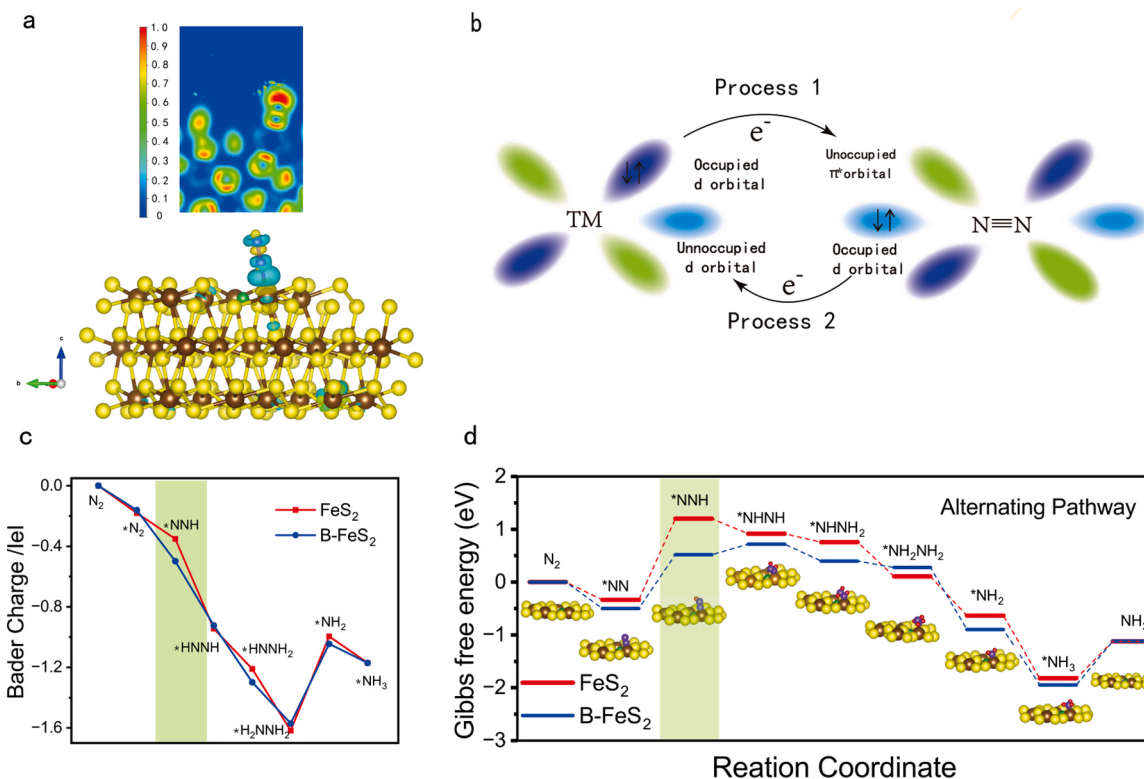


**Fig. 6.** (a) Electronic location function (ELF) and Charge density differences (Yellow implies charge accumulation and blue implies charge depletion; brown sphere: iron atom, green sphere: born atom, yellow sphere: sulfur atom, and blue sphere: nitrogen atom) of nitrogen adsorbed on the B-FeS<sub>2</sub>. (b) Schematic diagram of electron transfer between nitrogen and Fe sites. (c) Bader Charge of dinitrogen molecules on FeS<sub>2</sub> and B-FeS<sub>2</sub>. (d) Calculated free-energy diagram for alternating pathways on B-FeS<sub>2</sub> and FeS<sub>2</sub>.

calculations reveal that the B-mediation can facilitate the first-step hydrogenation of N<sub>2</sub> in the RDS of eNRR via reducing the energy barrier for \*NNH intermediate. Therefore, B-FeS<sub>2</sub> shows a high ammonia yield (1.56 mmol·g<sup>-1</sup>·h<sup>-1</sup>) with 12.6 % Faradaic efficiency at -1.4 V vs. Ag/AgCl. This strategy of d-band center mediation via the B atoms is an effective means to activate the reactant molecules and thus boost the catalytic activity. It can be applied to a lot of reactions to acquire the high-yield products except for eNRR, such as hydrogen evolution reaction (HER), carbon dioxide reduction reaction (CO<sub>2</sub>RR), electro-oxidation reaction (EOR), and oxygen evolution reaction (OER), etc.

#### 4. Conclusions

In conclusion, we designed a B-mediated FeS<sub>2</sub> as an efficient eNRR electrocatalyst via the modulation of d-band center. DFT theoretical calculations and experiments showed that the B-mediation can upshift the d-band center of FeS<sub>2</sub> nearly to the Fermi energy level. As a result, a strong d-π\* interaction between the π\* orbitals of nitrogen molecules and the 3d orbitals of the Fe sites occurred, thus contributing to a high eNRR rate of 1.56 mmol·g<sup>-1</sup>·h<sup>-1</sup> and a FE of 12.6 % for B-FeS<sub>2</sub>, outperforming most of eNRR catalysts. This work provides a new insight for the design of eNRR catalyst through the d-band center modulation.

#### CRediT authorship contribution statement

Hang Xiao: conceptualization, methodology, writing-review & editing. Mengyang Xia: validation, data curation, formal analysis. Ben Chong: software, data curation. He Li: resources, investigation. Bo Lin: writing – review & editing, funding acquisition, visualization. Guidong Yang: supervision, project administration, writing – review & editing.

#### Declaration of Competing Interest

The authors declare no conflict of interest.

#### Data availability

Data will be made available on request.

#### Acknowledgements

This work was supported by the National Key R&D Program of China (2020YFA0710000), Joint Funds of the National Natural Science Foundation of China (U22A20391), National Natural Science Foundation of China (Grant Nos. 22002014, 22078256, 22308272), the high-level innovation and entrepreneurship talent project of Qinchuangyuan (2021QCYRC4-24), the Key R&D Program of Shaanxi Province (2023-YBGY-323), Innovation Capability Support Program of Shaanxi (NO. 2023-CX-TD-26), and the “Young Talent Support Plan” of Xi'an Jiaotong University (HGJ6J021).

#### Appendix A. Supporting information

Supplementary data associated with this article can be found in the online version at doi:10.1016/j.apcatb.2023.123474.

#### References

- [1] J. Deng, J.A. Iniguez, C. Liu, Electrocatalytic nitrogen reduction at low temperature, Joule 2 (2018) 846–856, <https://doi.org/10.1016/j.joule.2018.04.014>.
- [2] Z. Lu, S.E. Saji, J. Langley, Y. Lin, Z. Xie, K. Yang, L. Bao, Y. Sun, S. Zhang, Y.H. Ng, L. Song, N. Cox, Z. Yin, Selective N<sub>2</sub>/H<sub>2</sub>O adsorption onto 2D amphiphilic amorphous photocatalysts for ambient gas-phase nitrogen fixation, Appl. Catal. B: Environ. 294 (2021), 120240, <https://doi.org/10.1016/j.apcatb.2021.120240>.

[3] Z. Wei, Z. Gu, Y. Zhang, K. Luo, S. Zhao, Phase-separated CuAg alloy interfacial stress induced Cu defects for efficient N<sub>2</sub> activation and electrocatalytic reduction, *Appl. Catal. B: Environ.* 320 (2023), 121915, <https://doi.org/10.1016/j.apcatb.2022.121915>.

[4] T. Li, S. Han, C. Wang, Y. Huang, Y. Wang, Y. Yu, B. Zhang, Ru-doped Pd nanoparticles for nitrogen electrooxidation to nitrate, *ACS Catal.* 11 (2021) 14032–14037, <https://doi.org/10.1021/acscatal.1c04360>.

[5] P. Shen, X. Li, Y. Luo, N. Zhang, X. Zhao, K. Chu, Ultra-efficient N<sub>2</sub> electroreduction achieved over a rhodium single-atom catalyst (Rh<sub>1</sub>/MnO<sub>2</sub>) in water-in-salt electrolyte, *Appl. Catal. B: Environ.* 316 (2022), 121651, <https://doi.org/10.1016/j.apcatb.2022.121651>.

[6] X. Wang, S. Li, Z. Yuan, Y. Sun, Z. Tang, X. Gao, H. Zhang, J. Li, S. Wang, D. Yang, J. Xie, Z. Yang, Y. Yan, Optimizing electrocatalytic nitrogen reduction via interfacial electric field modulation: elevating d-band center in WS<sub>2</sub>-WO<sub>3</sub> for enhanced intermediate adsorption, e202303794, *Angew. Chem. Int. Ed.* 62 (2023), <https://doi.org/10.1002/anie.202303794>.

[7] G. Qian, W. Lyu, X. Zhao, J. Zhou, R. Fang, F. Wang, Y. Li, Efficient photoreduction of diluted CO<sub>2</sub> to tunable syngas by Ni–Co dual sites through d-band center manipulation, *Angew. Chem. Int. Ed.* 61 (2022), e202210576, <https://doi.org/10.1002/anie.202210576>.

[8] Z. Ma, X. Liu, X. Wang, Z. Luo, W. Li, Y. Nie, L. Pei, Q. Mao, X. Wen, J. Zhong, Manipulating the d-band center enhances photoreduction of CO<sub>2</sub> to CO in Zn<sub>2</sub>GeO<sub>4</sub> nanorods, *Chem. Eng. J.* 468 (2023), 143569, <https://doi.org/10.1016/j.cej.2023.143569>.

[9] R. Gao, L. Pan, H. Wang, X. Zhang, L. Wang, J.-J. Zou, Ultradispersed nickel phosphide on phosphorus-doped carbon with tailored d-band center for efficient and chemoselective hydrogenation of nitroarenes, *ACS Catal.* 8 (2018) 8420–8429, <https://doi.org/10.1021/acscatal.8b02091>.

[10] M. Jin, R. Ando, M.J. Jellen, M.A. Garcia-Garibay, H. Ito, Encapsulating *N*-heterocyclic carbene binuclear transition-metal complexes as a new platform for molecular rotation in crystalline solid-state, *J. Am. Chem. Soc.* 143 (2021) 1144–1153, <https://doi.org/10.1021/jacs.0c11981>.

[11] Q. Wu, W. Yang, X. Wang, W. Zhu, S. Lv, Y. Zhou, T. Chen, S. Liu, W. Li, Z. Chen, Inherent vacancy of compressive Ru nanoparticles accelerate electro-catalytic hydrogen energy conversion, *Appl. Catal. B: Environ.* 335 (2023), 122896, <https://doi.org/10.1016/j.apcatb.2023.122896>.

[12] M.A. Mushtaq, A. Kumar, G. Yasin, M. Arif, M. Tabish, S. Ibraheem, X. Cai, W. Ye, X. Fang, A. Saad, J. Zhao, S. Ji, D. Yan, 3D interconnected porous Mo-doped WO<sub>3</sub>@CdS hierarchical hollow heterostructures for efficient photoelectrochemical nitrogen reduction to ammonia, *Appl. Catal. B: Environ.* 317 (2022), 121711, <https://doi.org/10.1016/j.apcatb.2022.121711>.

[13] X. Bai, L. Guo, T. Jia, D. Hao, C. Wang, H. Li, R. Zong, Perylene diimide growth on both sides of carbon nanotubes for remarkably boosted photocatalytic degradation of diclofenac, J. Hazard. Mater. 435 (2022), 128992, <https://doi.org/10.1016/j.jhazmat.2022.128992>.

[14] T. Ma, C. Yang, L. Guo, R.A. Soomro, D. Wang, B. Xu, F. Fu, Refining electronic properties of Bi<sub>2</sub>MoO<sub>6</sub> by In-doping for boosting overall nitrogen fixation via relay catalysis, *Appl. Catal. B: Environ.* 330 (2023), 122643, <https://doi.org/10.1016/j.apcatb.2023.122643>.

[15] Y. Kong, H. Kong, C. Lv, G. Chen, Engineering reductive iron on a layered double hydroxide electrocatalyst for facilitating nitrogen reduction reaction, *Adv. Mater. Interfaces* 9 (2022), 2102242, <https://doi.org/10.1002/admi.202102242>.

[16] W. Tong, B. Huang, P. Wang, Q. Shao, X. Huang, Exposed facet-controlled N<sub>2</sub> electroreduction on distinct Pt<sub>3</sub>Fe nanostructures of nanocubes, nanorods and nanowires, *Nat. Sci. Rev.* 8 (2021), <https://doi.org/10.1093/nsr/nwaa088>.

[17] M. Ma, X. Han, H. Li, X. Zhang, Z. Zheng, L. Zhou, J. Zheng, Z. Xie, Q. Kuang, L. Zheng, Tuning electronic structure of PdZn nanocatalyst via acid-etching strategy for highly selective and stable electrolytic nitrogen fixation under ambient conditions, *Appl. Catal. B: Environ.* 265 (2020), 118568, <https://doi.org/10.1016/j.apcatb.2019.118568>.

[18] J. Chen, G. Qian, B. Chu, Z. Jiang, K. Tan, L. Luo, B. Li, S. Yin, Tuning d-band center of Pt by PtCo-PtSn heterostructure for enhanced oxygen reduction reaction performance, *Small* 18 (2022), 2106773, <https://doi.org/10.1002/smll.202106773>.

[19] Y. Zhang, L. Ran, Y. Zhang, P. Zhai, Y. Wu, J. Gao, Z. Li, B. Zhang, C. Wang, Z. Fan, X. Zhang, J. Cao, D. Jin, L. Sun, J. Hou, Two-dimensional defective boron-doped niobic acid nanosheets for robust nitrogen photofixation, *ACS Nano* 15 (2021) 17820–17830, <https://doi.org/10.1002/gnnvmp>.

[20] D. Gao, B. Xia, C. Zhu, Y. Du, P. Xi, D. Xue, J. Ding, J. Wang, Activation of the MoSe<sub>2</sub> basal plane and Se-edge by B doping for enhanced hydrogen evolution, *J. Mater. Chem. A* 6 (2018) 510–515, <https://doi.org/10.1039/C7TA09982G>.

[21] F. Xu, D. Wu, Z. Wang, A. Ma, F. Wu, H. Xu, G. Fan, Synergistic effect and high performance of transition metal-anchored boron-doped graphyne electrocatalyst applied in the electroreduction of CO<sub>2</sub> to C<sub>1</sub> products: a DFT study, *Appl. Surf. Sci.* 631 (2023), 157505, <https://doi.org/10.1016/j.apsusc.2023.157505>.

[22] Y. Chen, K. Yang, B. Jiang, J. Li, M. Zeng, L. Fu, Emerging two-dimensional nanomaterials for electrochemical hydrogen evolution, *J. Mater. Chem. A* 5 (2017) 8187–8208, <https://doi.org/10.1039/C7TA00816C>.

[23] S. Chen, X. Liu, J. Xiong, L. Mi, X.-Z. Song, Y. Li, Defect and interface engineering in metal sulfide catalysts for the electrocatalytic nitrogen reduction reaction: a review, *J. Mater. Chem. A* 10 (2022) 6927–6949, <https://doi.org/10.1039/D2TA00070A>.

[24] B. Liu, Y. Zheng, H.-Q. Peng, B. Ji, Y. Yang, Y. Tang, C.-S. Lee, W. Zhang, Nanostructured and boron-doped diamond as an electrocatalyst for nitrogen fixation, *ACS Energy Lett.* 5 (2020) 2590–2596, <https://doi.org/10.ggz5kv>.

[25] H.-B. Wang, J.-Q. Wang, R. Zhang, C.-Q. Cheng, K.-W. Qiu, Y. Yang, J. Mao, H. Liu, M. Du, C.-K. Dong, X.-W. Du, Bionic design of a Mo(IV)-doped FeS<sub>2</sub> catalyst for electroreduction of dinitrogen to ammonia, *ACS Catal.* 10 (2020) 4914–4921, <https://doi.org/10.gnnxpt>.

[26] H. Li, M. Xia, B. Chong, H. Xiao, B. Zhang, B. Lin, B. Yang, G. Yang, Boosting photocatalytic nitrogen fixation via constructing low-oxidation-state active sites in the nanoconfined spinel iron cobalt oxide, *ACS Catal.* 12 (2022) 10361–10372, <https://doi.org/10.1021/acscatal.2c02282>.

[27] H. Du, C. Yang, W. Pu, L. Zeng, J. Gong, Enhanced electrochemical reduction of N<sub>2</sub> to ammonia over pyrite FeS<sub>2</sub> with excellent selectivity, *ACS Sustain. Chem. Eng.* 8 (2020) 10572–10580, <https://doi.org/10.gnnxp>.

[28] L. Gao, C. Guo, M. Zhao, H. Yang, X. Ma, C. Liu, X. Liu, X. Sun, Q. Wei, Electrocatalytic N<sub>2</sub> reduction on FeS<sub>2</sub> nanoparticles embedded in graphene oxide in acid and neutral conditions, *ACS Appl. Mater. Interfaces* 13 (2021) 50027–50036, <https://doi.org/10.gnnxpq>.

[29] S. Erfeldt, M. Petersson, A. Palmqvist, Alumina-supported In<sub>2</sub>O<sub>3</sub>, Ga<sub>2</sub>O<sub>3</sub> and B<sub>2</sub>O<sub>3</sub> catalysts for lean NO<sub>x</sub> reduction with dimethyl ether, *Appl. Catal. B: Environ.* 117–118 (2012) 369–383, <https://doi.org/10.1016/j.apcatb.2012.01.031>.

[30] H. Li, P. Wen, Q. Li, C. Dun, J. Xing, C. Lu, S. Adhikari, L. Jiang, D.L. Carroll, S. M. Geyer, Earth-abundant iron diboride (FeB<sub>2</sub>) nanoparticles as highly active bifunctional electrocatalysts for overall water splitting, *Adv. Energy Mater.* 7 (2017), 1700513, <https://doi.org/10.1002/aenm.201700513>.

[31] H. Xiao, T. Wei, X. Ren, B. Lin, G. Yang, PtS quantum dots/Nb<sub>2</sub>O<sub>5</sub> nanosheets with accelerated charge transfer for boosting photocatalytic H<sub>2</sub> production, *Nanoscale* 14 (2022) 12403–12408, <https://doi.org/10.1039/D2NR03112D>.

[32] B. Lin, G. Yang, L. Wang, Stacking-layer-number dependence of water adsorption in 3D ordered close-packed g-C<sub>3</sub>N<sub>4</sub> nanosphere arrays for photocatalytic hydrogen evolution, *Angew. Chem. Int. Ed.* 58 (2019) 4587–4591, <https://doi.org/10.gjviv3>.

[33] X. Yan, B. Xu, X. Yang, J. Wei, B. Yang, L. Zhao, G. Yang, Through hydrogen spillover to fabricate novel 3DOM-H<sub>x</sub>WO<sub>3</sub>/Pt/CdS Z-scheme heterojunctions for enhanced photocatalytic hydrogen evolution, *Appl. Catal. B: Environ.* 256 (2019), 117812, <https://doi.org/10.1016/j.apcatb.2019.117812>.

[34] J. Wang, B. Huang, Y. Ji, M. Sun, T. Wu, R. Yin, X. Zhu, Y. Li, Q. Shao, X. Huang, A general strategy to glassy M-Te (M = Ru, Rh, Ir) porous nanorods for efficient electrochemical N<sub>2</sub> fixation, *Adv. Mater.* 32 (2020), 1907112, <https://doi.org/10.1002/adma.201907112>.

[35] Y. Ren, C. Yu, X. Han, X. Tan, Q. Wei, W. Li, Y. Han, L. Yang, J. Qiu, Methanol-mediated electrosynthesis of ammonia, *ACS Energy Lett.* 6 (2021) 3844–3850, <https://doi.org/10.gpj8fs>.

[36] X. Ren, M. Xia, B. Chong, X. Yan, N. Wells, G. Yang, Uniform NiP<sub>x</sub> nanospheres loaded onto defective H<sub>x</sub>WO<sub>3-y</sub> with three-dimensionally ordered macroporous structure for photocatalytic nitrogen reduction, *Appl. Catal. B: Environ.* 297 (2021), 120468, <https://doi.org/10.1016/j.apcatb.2021.120468>.

[37] Y. Zhao, Y. Zhao, R. Shi, B. Wang, G.I.N. Waterhouse, L. Wu, C. Tung, T. Zhang, Tuning oxygen vacancies in ultrathin TiO<sub>2</sub> nanosheets to boost photocatalytic nitrogen fixation up to 700 nm, *Adv. Mater.* 31 (2019), 1806482, <https://doi.org/10.1002/adma.201806482>.

[38] N. Zhang, A. Jalil, D. Wu, S. Chen, Y. Liu, C. Gao, W. Ye, Z. Qi, H. Ju, C. Wang, X. Wu, L. Song, J. Zhu, Y. Xiong, Refining defect states in W<sub>18</sub>O<sub>49</sub> by Mo doping: a strategy for tuning N<sub>2</sub> activation towards solar-driven nitrogen fixation, *J. Am. Chem. Soc.* 140 (2018) 9434–9443, <https://doi.org/10.1021/jacs.8b02076>.

[39] M. Wang, S. Liu, H. Ji, T. Yang, T. Qian, C. Yan, Salting-out effect promoting highly efficient ambient ammonia synthesis, *Nat. Commun.* 12 (2021) 3198, <https://doi.org/10.gk263n>.

[40] L. Zhang, H. Zhou, X. Yang, S. Zhang, H. Zhang, X. Yang, X. Su, J. Zhang, Z. Lin, Boosting electroreduction kinetics of nitrogen to ammonia via atomically dispersed Sn protuberance, *Angew. Chem. Int. Ed.* 62 (2023), e202217473, <https://doi.org/10.1002/anie.202217473>.

[41] X. Guo, J. Gu, S. Lin, S. Zhang, Z. Chen, S. Huang, Tackling the activity and selectivity challenges of electrocatalysts toward the nitrogen reduction reaction via atomically dispersed Bi atom catalysts, *J. Am. Chem. Soc.* 142 (2020) 5709–5721, <https://doi.org/10.1021/jacs.9b13349>.

[42] J.-C. Liu, X.-L. Ma, Y. Li, Y.-G. Wang, H. Xiao, J. Li, Heterogeneous Fe<sub>3</sub> single-cluster catalyst for ammonia synthesis via an associative mechanism, *Nat. Commun.* 9 (2018) 1610, <https://doi.org/10.1038/s41467-018-03795-8>.

[43] G. Zhou, T. Li, R. Huang, P. Wang, B. Hu, H. Li, L. Liu, Y. Sun, Recharged catalyst with memristive nitrogen reduction activity through learning networks of spiking neurons, *J. Am. Chem. Soc.* 143 (2021) 5378–5385, <https://doi.org/10.1021/jacs.0c12458>.

[44] Y. Li, J. Li, J. Huang, J. Chen, Y. Kong, B. Yang, Z. Li, L. Lei, G. Chai, Z. Wen, L. Dai, Y. Hou, Boosting electroreduction kinetics of nitrogen to ammonia via tuning electron distribution of single-atomic iron sites, *Angew. Chem. Int. Ed.* 133 (2021) 9160–9167, <https://doi.org/10.1002/ange.202100526>.

[45] L. Li, W. Yu, W. Gong, H. Wang, C.-L. Chiang, Y. Lin, J. Zhao, L. Zhang, J.-M. Lee, G. Zou, Sulfur-induced electron redistribution of single molybdenum atoms promotes nitrogen electroreduction to ammonia, *Appl. Catal. B: Environ.* 321 (2023), 122038, <https://doi.org/10.1016/j.apcatb.2022.122038>.

[46] K. Hu, P. Qiu, L. Zeng, S. Hu, L. Mei, S. An, Z. Huang, X. Kong, J. Lan, J. Yu, Z. Zhang, Z. Xu, J.K. Gibson, Z. Chai, Y. Bu, W. Shi, Solar-driven nitrogen fixation catalyzed by stable radical-containing MOFs: improved efficiency induced by a structural transformation, *Angew. Chem. Int. Ed.* 59 (2020) 20666–20671, <https://doi.org/10.1002/anie.202009630>.

[47] D. Malko, A. Kucernak, Kinetic isotope effect in the oxygen reduction reaction (ORR) over Fe-N/C catalysts under acidic and alkaline conditions, *Electrochim. Commun.* 83 (2017) 67–71, <https://doi.org/10.1016/j.elecom.2017.09.004>.

[48] P. Liu, Y. Zhao, R. Qin, S. Mo, G. Chen, L. Gu, D.M. Chevrier, P. Zhang, Q. Guo, D. Zang, B. Wu, G. Fu, N. Zheng, Photochemical route for synthesizing atomically dispersed palladium catalysts, *Science* 352 (2016) 797–800, <https://doi.org/10.1126/science.aaf5251>.

[49] L. Yang, C. Cheng, X. Zhang, C. Tang, K. Du, Y. Yang, S.-C. Shen, S.-L. Xu, P.-F. Yin, H.-W. Liang, T. Ling, Dual-site collaboration boosts electrochemical nitrogen reduction on Ru-S-C single-atom catalyst, *Chin. J. Catal.* 43 (2022) 3177–3186, [https://doi.org/10.1016/S1872-2067\(22\)64136-6](https://doi.org/10.1016/S1872-2067(22)64136-6).

[50] R. Liu, H. Fei, J. Wang, T. Guo, F. Liu, J. Wang, Z. Wu, D. Wang, Insights of active sites separation mechanism for highly efficient electrocatalytic N<sub>2</sub> reduction to ammonia over glucose-induced metallic MoS<sub>2</sub>, *Appl. Catal. B: Environ.* 337 (2023), 122997, <https://doi.org/10.1016/j.apcatb.2023.122997>.